Supplementary Information

RobInHood: A Robotic Chemist in a Fume Hood

Section 1: Module Design

Table S1: Summary table of RobInHood modules.

Module Name	Module Purpose / Brief Description	Relevant Figures
Robot arm	Seven-degree-of-freedom Emika Panda arm with custom fingertips to allow reliable gripping of vials, filter and Quantos cartridges.	Figure S1
Vial storage	Storing both empty vials and samples in the workflow.	Figure S4
Liquid dispensing	Syringe pump mechanism capable of dispensing up to nine separate liquids, contains two separate syringe pumps (Tecan Cavro XCalibur, TriContinent C3000MP).	Figures S5 - S6 Figure S10
Stirrer bar dispensing	Geneva wheel mechanism for dispensing stirrer bars.	Figure S11
Capping/Decapping	Caps and de-caps 20 ml reaction vials.	Figure S7
Solid dispensing	Mettler Toledo Quantos and cartridge system for dispensing solids, can store up to 10 cartridges.	Figure S3 Figure S8
Heating and stirring	Heating and stirring samples, a hotplate (IKA RCT digital) with a custom aluminium heating block.	Figure S2 Figure S9
Vision-based analysis	Custom lightbox with a camera (ELP USB Camera Module with 100 degree lens) and white LED for imaging samples.	Figure S12
Filtration	Pneumatically controlled vacuum filtration module with exchangeable custom PTFE filter cartridges. Filtrate recovery and system cleaning are achieved via a syringe pump (Tecan Cavro XCalibur).	Figures S13-S19

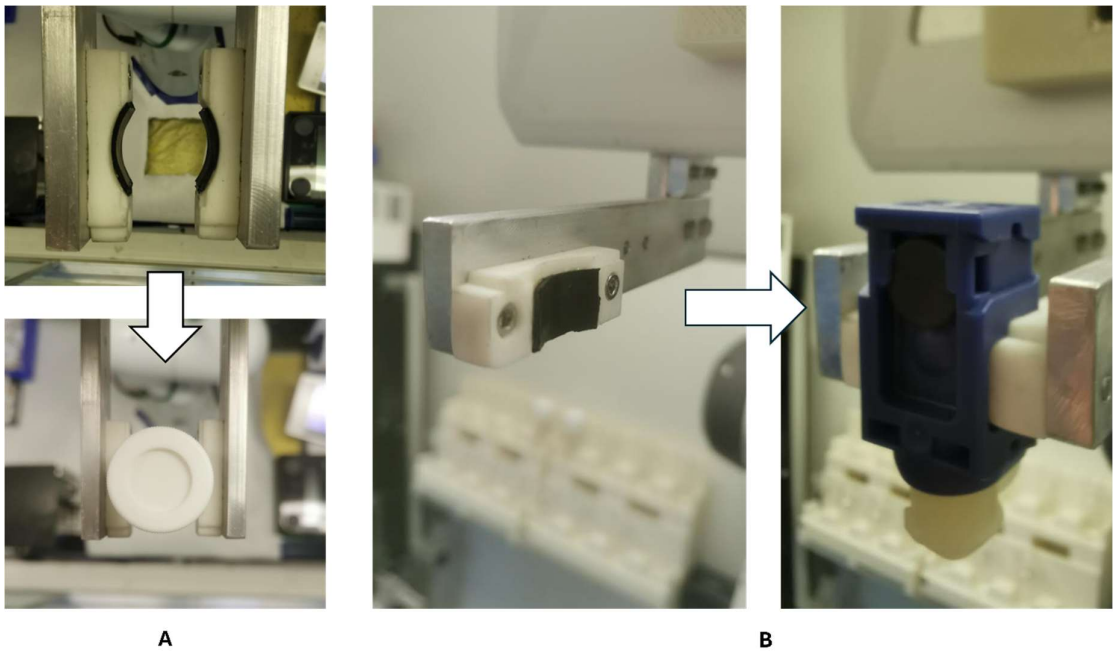

Figure S1: Multipurpose fingertips for the Franka Emika Panda. A. The two concave fingertips of the robot, lined with rubber, allowing the gripper to hold vials firmly. B. Keyed features in the tips, designed around the existing Mettler Toledo Quantos cartridges, allowing the same set of fingertips to securely grip them.

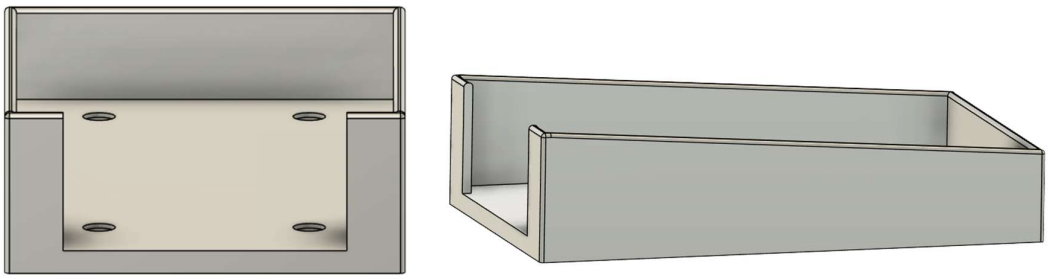

Figure S2: IKA hotplate adaptor to allow mounting in a fixed position to the fume hood breadboard.

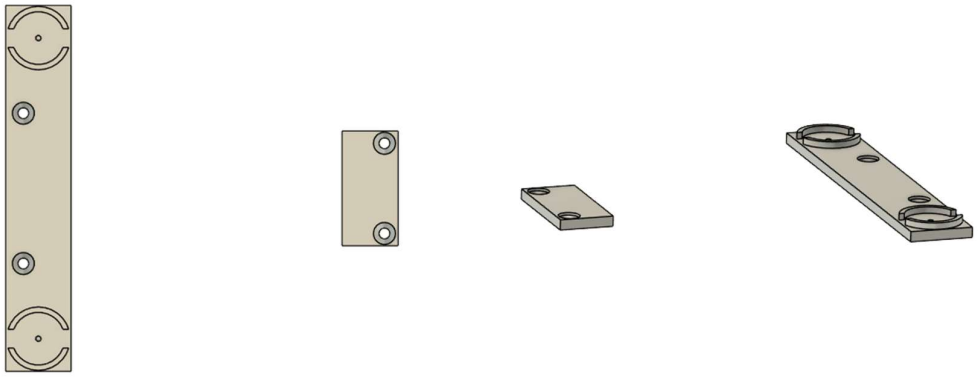

Figure S3: Adaptor for the Mettler-Toledo Quantos system. The countersunk holes allow mounting to the breadboard, whereas the raised sections secure the Quantos levelling feet while still permitting adjustment for levelling.

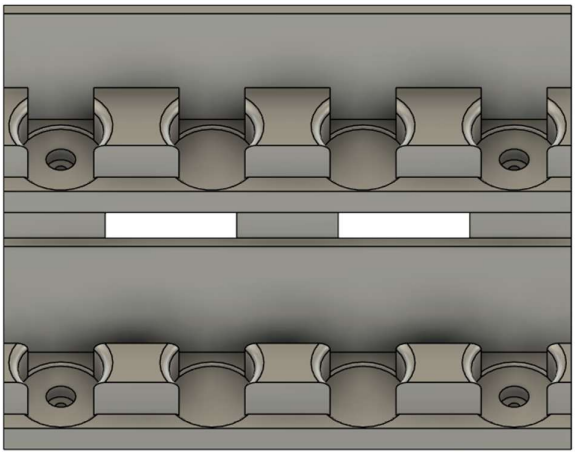

Figure S4: Vial rack for 8 x 20 mL vials.

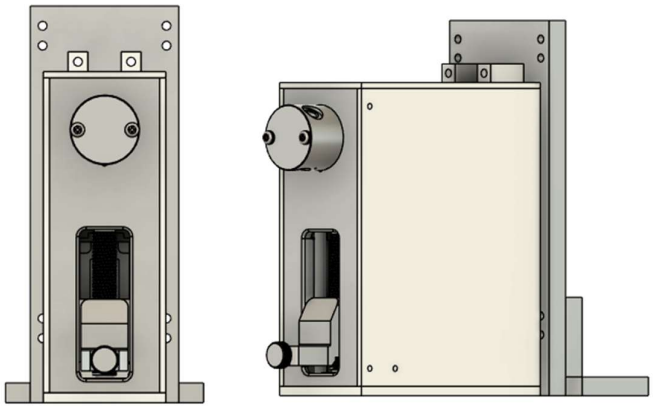

Figure S5: Case and extrusion mount for the XCalibur (Tecan Cavro) syringe pump.

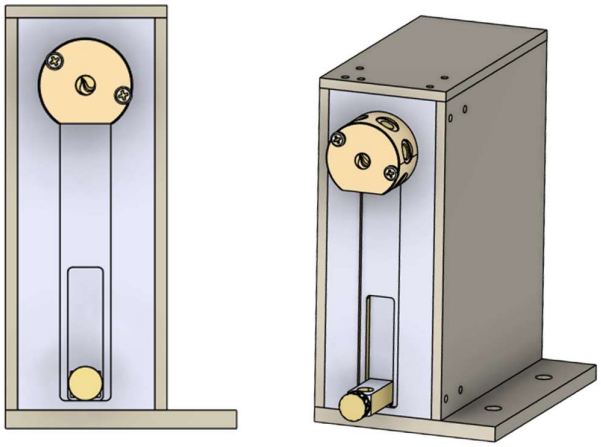

Figure S6: Case and extrusion mount for the C3000MP (TriContinent) syringe pump.

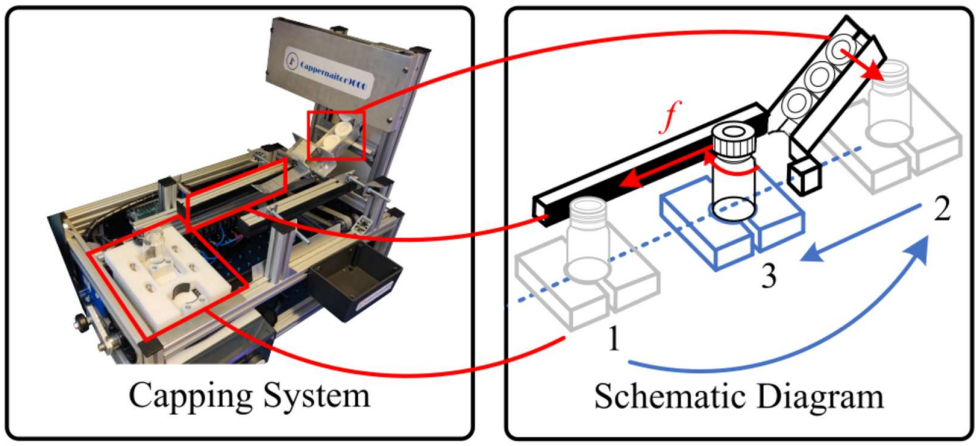

Figure S7: Photograph and schematic of the capping-decapping system. The vial is placed by the PANDA robot, and the capping/decapping process is achieved via friction with the rail. Reproduced from.[1]

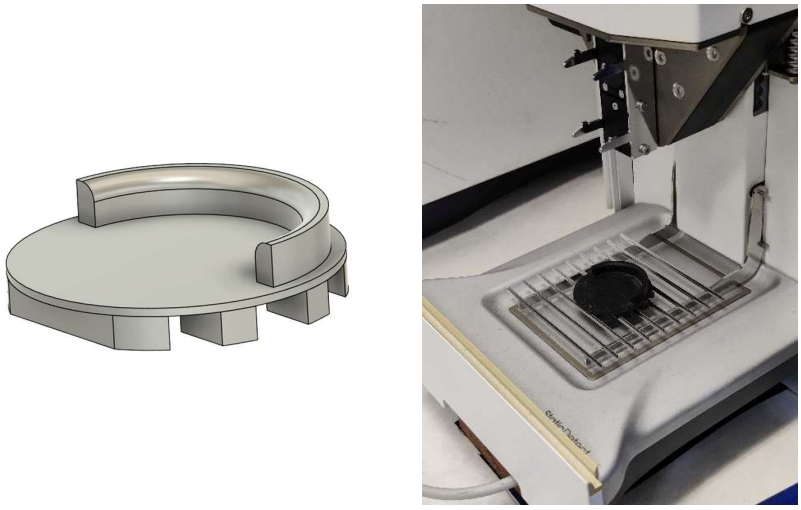

Figure S8: Vial adaptor allowing for consistent placement onto the Quantos solid dispenser.

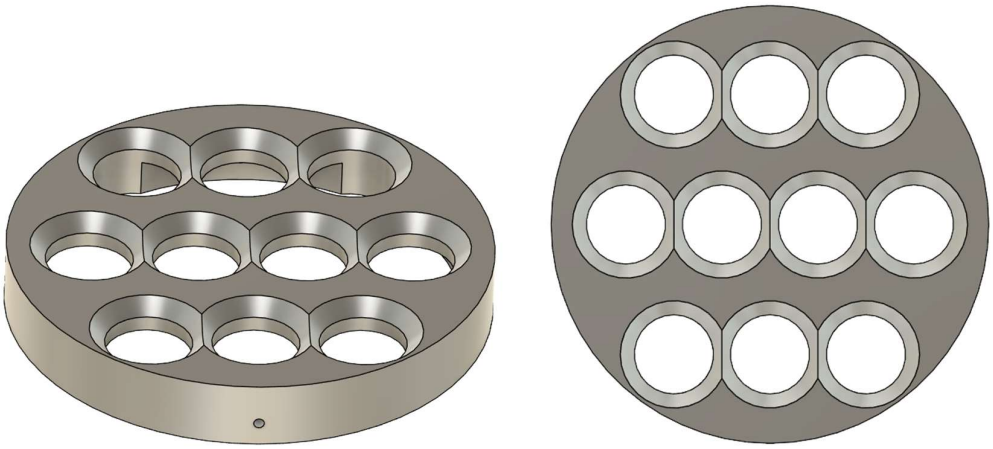

Figure S9: The IKA hotplate heating block adaptor, allowing 10 x 20 mL vials to be placed repeatably on a hotplate.

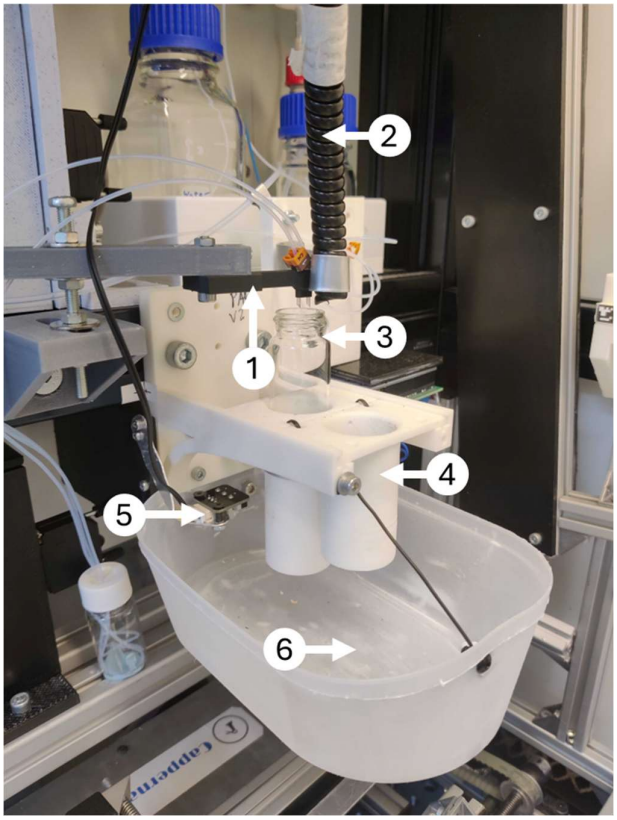

Figure S10: Actuated Holder design. 1 – Tubing head holding dispense tubing from both pumps. 2. Stirrer bar dispenser chute. 3. 40 mL vial for collecting wash / prime waste. 4. Sample vial position. 5. Microswitch to activate stirrer bar dispenser (Figure S11). 6. Spill/Safety tray.

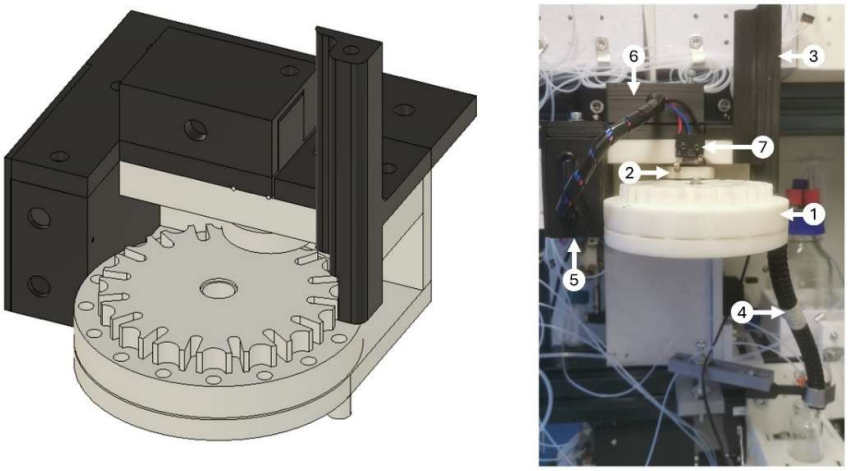

Figure S11: Stirrer bar dispenser. A. CAD model of the dispenser, the black part is fabricated of ABS while the beige one is fabricated from resin. B Bars dispenser installed in RobInHood. 1 – Geneva wheel. This wheel also contains the stirrer bars. 2 – Geneva wheel drive. This mechanism requires minimal torque, allowing the use of a small motor with reduced consumption of current, allowing the device to be powered by only a USB port from Arduino UNO used to control the dispenser. 3 – Stirrer bars hopper. 4 – Chute. 5 – Arduino UNO. 6 – Motor. 7 – Limit switch.

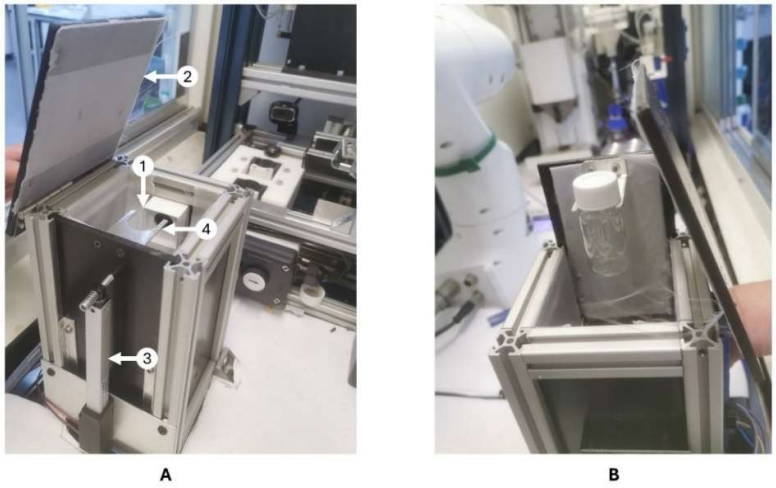

Figure S12: Lightbox. A. The lightbox shown in the picture is designed to provide consistency when taking photographs by using LED lights at the bottom of the box to illuminate the interior once it is closed.1 – Fish-eye lens camera (ELP USB Camera Module with 100 degree lens). This camera allows taking pictures from a close distance, which results in a reduced size of the lightbox. 2 – Liftable top. 3 – A linear actuator is used to open and close the top while simultaneously lifting and lowering the vial holder, where the robot can place a sample to be analysed. 4 – Vial holder. B. A vial is placed in the holder of the lightbox.

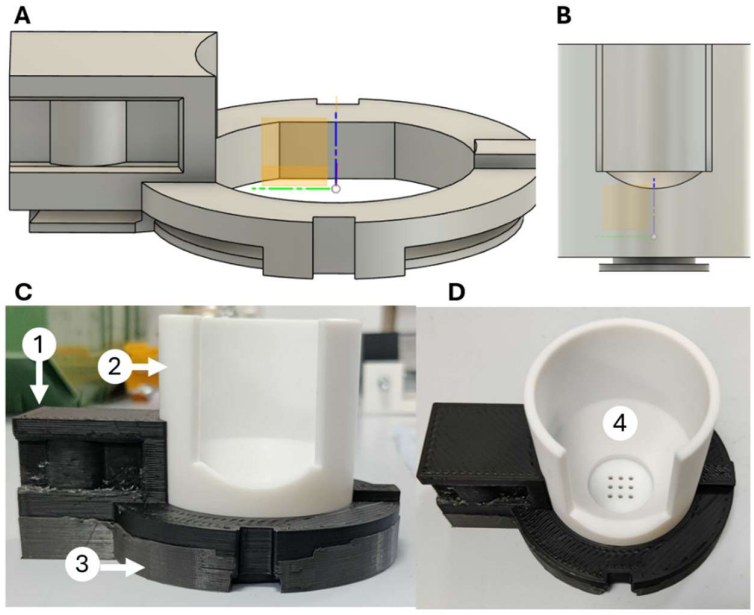

Figure S13: Filtration cartridge. A. STL of the filtration cartridge collar. The bottom of the collar has a dovetail to retain the rubber gasket. B. STL of the filtering vessel and splash guard. The bottom has an overhang to retain the rubber gasket. C. Example of the filtration cartridge. 1 – Cartridge collar (ABS). 2. Filtration vessel and splash guard (PTFE). 3. Rubber gasket. D. Alternative view of the filtration vessel showing the rigid support plate for the filter paper/ membrane (4).

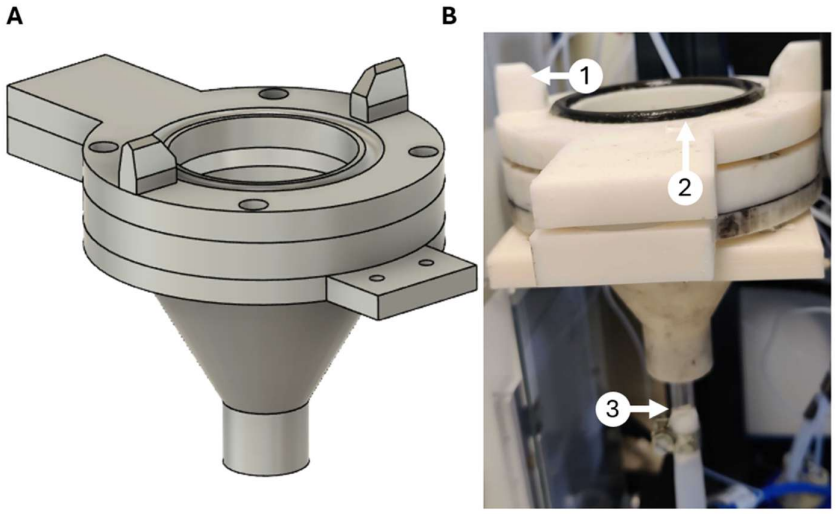

Figure S14: Filtration station filter funnel. A. STL of the filter funnel design. B. Filter funnel in RobInHood. 1 – Locator pins to allow consistent cartridge placement. 2 – O-ring for vacuum seal. 3 – Enclosed glass filter funnel.

Figure S15: Receiving flask in the filtration station. 1 – 6 mm outer diameter PTFE connection to the filtration funnel. 2 – 1.6 mm outer diameter PTFE connection to the pump for sample recovery and washing. 3 – 6 mm pneumatic connection to the vacuum generator.

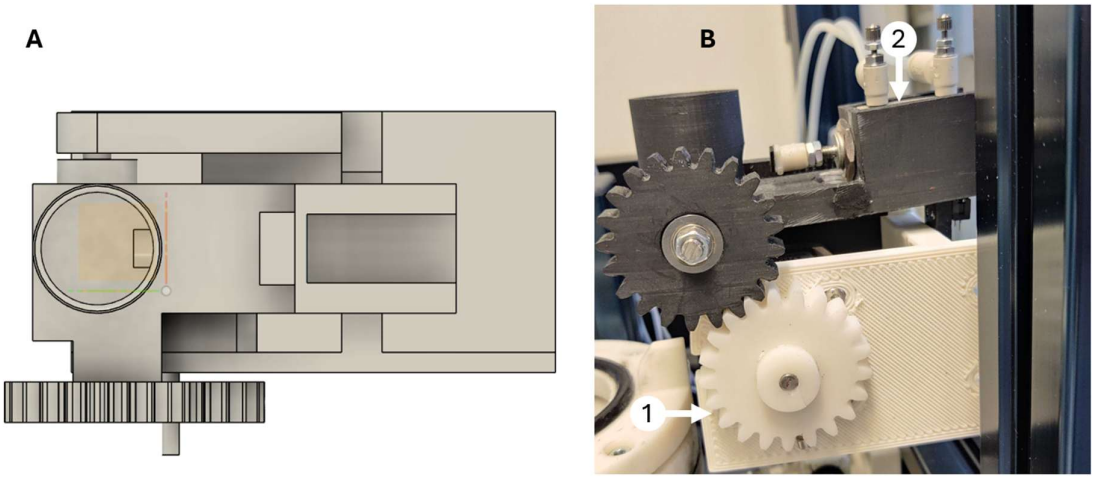

Figure S16: Pouring arm in the filtration station. A. STL of the pouring arm. B. Pouring arm in RobInHood. 1- Drive gear to the stepper motor for the pouring motion. 2- Pneumatic piston to clamp the vial.

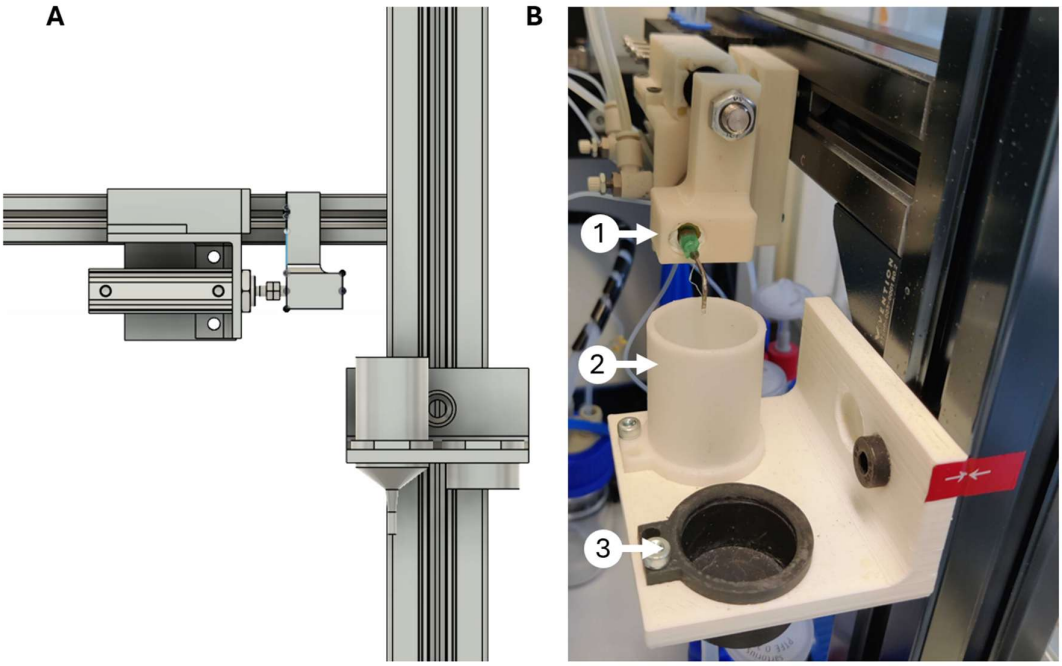

Figure S17: Filtration station receiving vial assembly. A. STL of the assembly. B. Assembly in RobInHood. 1 – actuated dispense head/output needle. 2 – Funnel to waste for needle washing. 3. Holder for the receiving vial.

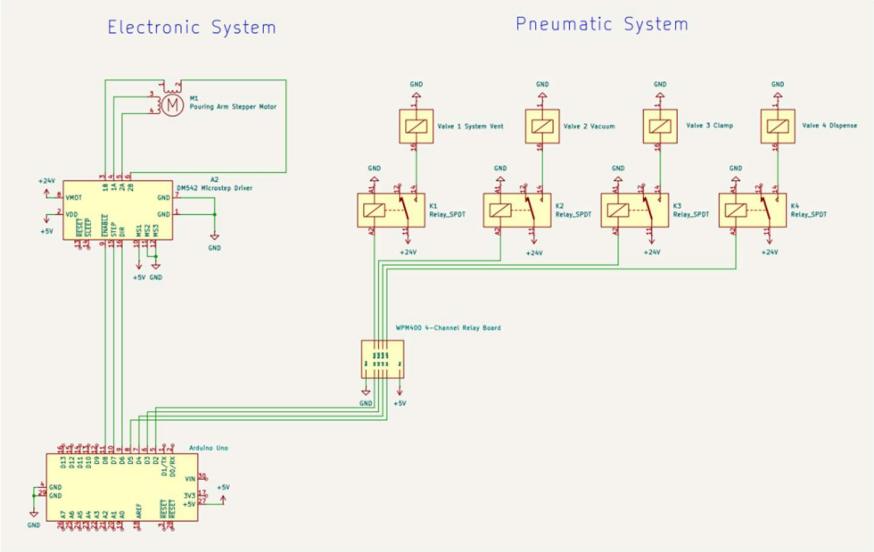

Figure S18: Electronic schematic of the filtration module. The Arduino Uno is connected to the RobInHood lab pc which communicates to the system through serial commands. A DM542 Microstep Driver controls the pouring arm. The Arduino is also connected to 4 relays on a WPM400 relay board that controls the valves on the pneumatic system, vial clamping, vacuum, needle movement, and system venting (**Figure S19**).

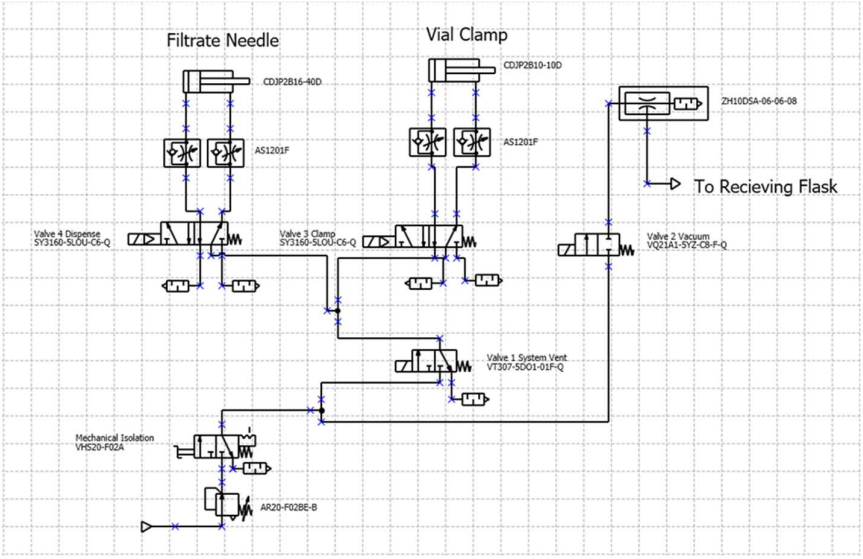

Figure S19: Pneumatic schematic of the filtration. A manual 3/2 valve is used to mechanically isolate the entire system. This is coupled with a solenoid controlled 3/2 valve which can be used to vent the system electronically. The pistons for vial clamping and the filtrate recovery needle are each controlled by a solenoid actuated 5/2 valve. The vacuum to the receiving flask is controlled by a 2/2 valve. The electrical system controlling the solenoids is described in **Figure S18**.

Section 2: Module Calibration

2.1 Liquid Dispensing Module

2.1.1 Cross-contamination Testing

To reduce time between dispensing different liquids and to minimise solvent/stock waste, it was necessary to construct a washing procedure that minimised both washing volumes and cross contamination. The dispense tubing volume is approximately 0.4 mL, syringe volume is 1 mL. Therefore, to wash and prime the tubing connected to the dispensing needle, the pump does the following sequence:

1. The pump aspirates 2 mL of volume from the reagent tubing line and dispenses it into waste, clearing the line from whatever solvent was present before.
2. The pump dispenses 1 mL of volume of the washing/priming solvent into the dispense tubing, with the overspill being captured in the waste vial (**Figure S10** -3).
3. The pump then aspirates 2 mL of volume from the dispense tube into the waste.
4. Steps 2 and 3 are repeated.
5. The pump then dispenses a further 1 mL of solvent into the dispense line.

UV/VIS spectroscopy was then used to measure potential cross-contamination while dispensing using the Tecan XCalibur pump with this washing procedure. All spectra were measured on a Shimadzu UV-2600i. Initially the spectra of a control series of methyl orange dye samples of known concentrations (0.1 – 10 ppm) were recorded (**Figure S20** A). These showed a detectable limit of below 0.1 ppm (0.1 mg / L) based on the peak at approximately 460 nm. The pump was then used to dispense 5 mL of 10 ppm methyl orange solution, followed by the washing procedure and then a 10 mL distilled water sample (RobInHood Wash procedure - green line **Figure S20** B). The spectra of a control sample, where 5 mL of 10 ppm methyl orange solution was dispensed, followed by 4 mL of distilled water, followed by a 10 mL distilled water sample (4 mL Wash Control – orange line **Figure S20** B), is also shown. Both the control and the RobInHood wash procedure sample appear flat in the 350-600 nm region, indicating that no cross contamination has occurred.

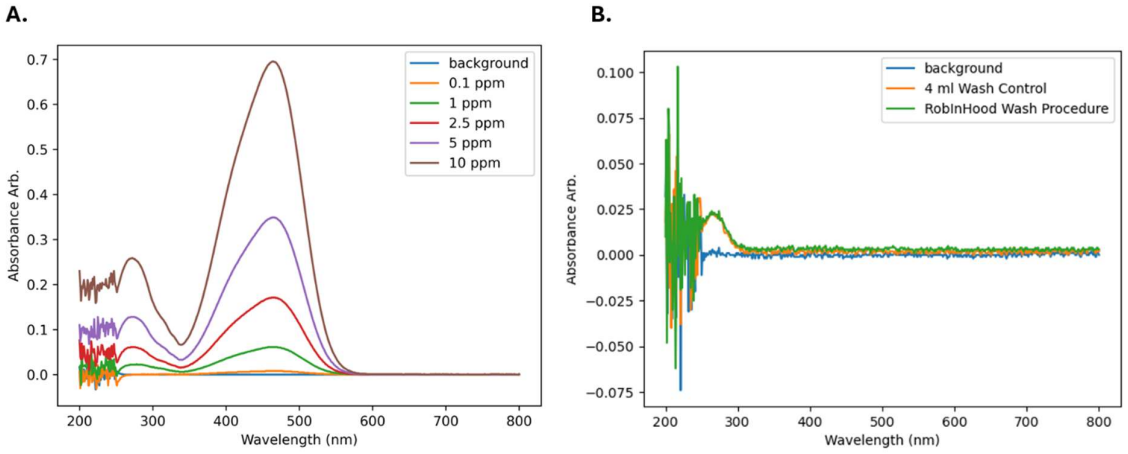

Figure S20: A. UV/VIS spectra of methyl orange standards in distilled water (0.1-10 ppm). B. UV/VIS spectra of a 10 mL distilled water samples while confirming the efficacy of the washing procedure.

2.1.2 Pump Dispense Accuracy Testing

Pump accuracy was measured gravimetrically using distilled water (lab source), with a distilled water reference density at 25 °C and atmospheric pressure of 0.997 g / mL.[2] The XCalibur used default dispensing conditions (set speed = 11), the C3000MP used set speed = 20 and a 1-second wait time between aspiration and dispensing. Error bars represent twice the standard error on six repeats per specified volume.

Table S2: Pump accuracy validation for the Tecan Cavro XCalibur and C3000MP Tricontinnent.

Specified Volume (uL)	Actual Volume XCalibur (µL)	Actual Volume C3000MP (uL)
50	48 ± 2.94	48 ± 2.84
250	248 ± 3.42	247 ± 1.97
500	497 ± 3.68	496 ± 1.64
750	748 ± 1.65	744 ± 4.14
1000	998.7 ± 2.23	994 ± 4.69

2.2 Solid Dispensing Module

It has been reported that the presence of external magnetic fields can cause reading errors on balances. As many workflows involve mixing by means of stirrer bars, the effect of the magnetic field caused by these stirrer bars on the Quantos mass balance was measured. The balance was zeroed and antistatic run for 2 minutes prior to measurement. A clean stirrer bar was measured, rotated 90 degrees and then measured again. This is to simulate the effect on the recorded weight of inconsistent stirrer bar positions between different samples. Two stirrer bar sizes were measured, 15 x 6 mm (**Table S3)** and 10 x 6 mm (**Table S4**). 10 repeats of each size were measured.

Results showing the effect of inconsistent magnetic stirrer bar placement on measurement accuracy. An average mass difference of 1.39 ± 0.25 mg was observed for 15 x 6 mm samples. An average mass difference of 0.43 ± 0.17 mg was observed 10 x 6 mm.

Table S3: Effect of magnetic stirrer bars on balance accuracy – 15 x 6 mm stirrer bars

Sample	Mass (mg)	Mass (mg)	Difference (mg)
1	1281.1	1279.8	-1.3
2	1317.7	1319.3	1.6
3	1309.8	1308.9	-0.9
4	1303.6	1305	1.4
5	1279	1280.4	1.4
6	1301.1	1299.8	-1.3
7	1291.1	1289.7	-1.4
8	1282.6	1284	1.4
9	1282.1	1283.4	1.3
10	1279.4	1277.5	-1.9

Table S4: Effect of magnetic stirrer bars on balance accuracy – 10 x 6 mm stirrer bars

Sample	Mass (mg)	Mass (mg)	Difference (mg)
1	763.7	762.9	-0.8
2	799.8	799.5	-0.3
3	793.6	793.1	-0.5
4	783.5	783.7	0.2
5	760.6	760	-0.6
6	796.2	795.8	-0.4
7	793.3	793	-0.3
8	787.2	786.8	-0.4
9	795.6	796	0.4
10	795.6	796	0.4

2.3 Filtration Cartridge Materials Compatibility Testing

To test the compatibility of the resin cartridges used in the dye-based porosity screening workflow. 6 x 6 x 6 mm cubes of the Formlabs V4 white resin white resin were printed, washed in isopropanol for 20 minutes before being cured at 60 °C for 30 minutes. These cubes were then each suspended in 2 mL of 99.8 atom % D_2O for the time indicated on the graph, before the solution was analysed by NMR. The spectra remain featureless with the exception of a peak at 4.7 ppm, which was due to the solvent [3].

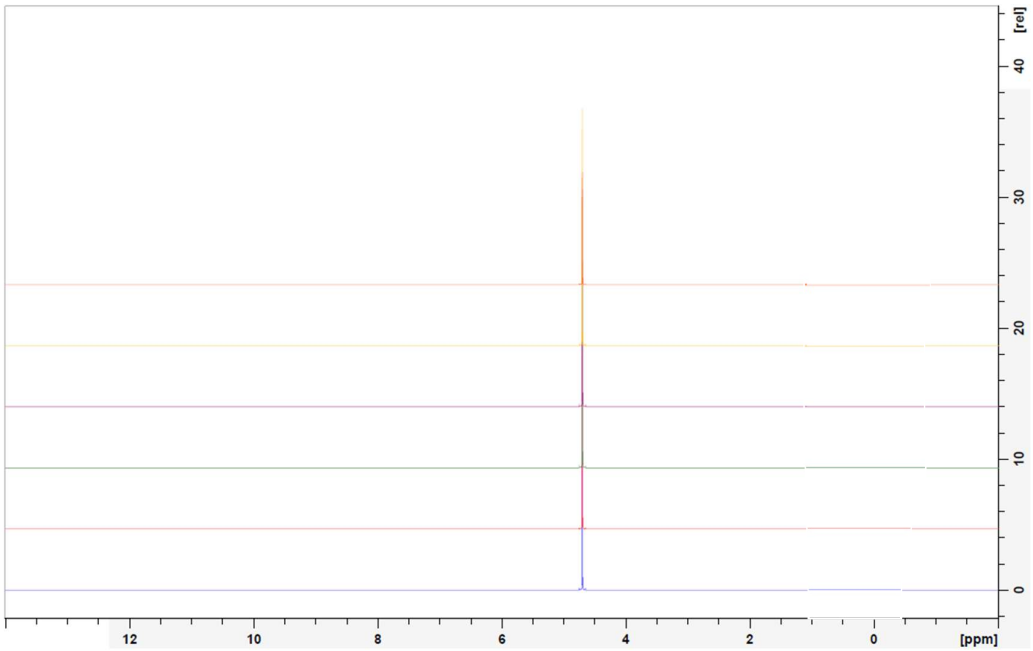

Figure S21: ^1H NMR (400 MHz, D_2O) contamination testing of Formlabs V4 white resin. The spectra remain featureless with the exception of a peak at 4.7 ppm, which was due to the solvent.[3]

2.4 Dye-based Porosity Screening Calibration

The previous work on the dye-based porosity screen was conducted under different conditions, in a different lightbox. [4] Therefore, to ensure meaningful results careful calibration is needed. When using different measurement systems for evaluating a common property, cross-calibration is crucial to ensure the reproducibility of results and measurements. Since our system differs in terms of lighting conditions and camera settings from those presented in the previous work,[4] we have developed a dedicated method for cross-calibration. This method is important because it can ensure reproducibility, regardless of whether the lightbox, camera or both are changed. To this end, we manually prepared six calibration samples with known concentrations (1, 2, 4, 6, 8, and 10 ppm) for each of the six dyes, as illustrated in **Figure S22-A,** that serve as the common entity to be measured.

Additionally, from the resulting images, we selected a Region of Interest (ROI) for all calibration samples. The mean of each ROI was calculated, aiming to make the measurement robust against noise. Next, we analysed the measurements taken from the ROI using Red, Green, Blue (RGB), Hue, Saturation, Value (HSV), CIELAB (LAB) colour spaces, and grey scale to identify which channel produced data more suitable to be used for fitting a curve, resulting in selecting channels: A from LAB, B from RGB, S from HVS, L for LAB, grey scale, and B from RGB for dye 1 to 6, respectively (**Figure S22-B**). Then, we identified curves that best fit the data, namely those that exhibit minimal fitting error and avoid multiple solutions for the same ppm value. To achieve this, we selected the following equation, which generates curves that fit the shape of the data while maintaining minimal error:

$$f(x) = \frac{A}{B + (Cx + D)^3}$$

Where A is a scaling factor, B shifts the denominator baseline, C scales the input concentration *x* (ppm*),* and D shifts the input before cubing. The coefficients A, D, C, and D can be tuned to fit the values given by each dye calibration sample series. Once the coefficients have been calculated by fitting the curve, an inverse function is necessary to predict ppm given the input in pixels (**Figure S23**). The inverse function is given by the following equation:

$$ppm = \frac{\left(\sqrt[3]{\left(\frac{A}{pixels}\right) - B} - D \right)}{C}$$

A limitation of this approach is observed near 0 and 10 ppm, the camera perception saturates at both ends of the scale, where the colour channels display a linear behaviour followed by a plateau, making the ROI measurements less reliable. The associated errors are summarised in **Table S5**. It can be observed that the Mean Squared Errors (MSEs) with exception of dye 4 are low, while the coefficient of determination R^2 indicates goodness of fit; for dye 1, dye 3 and dye 5, $R^2 >$ 0.96 therefore it indicates excellent fit, for dye 2 and dye 6 $R^2 \sim 0.83–0.86$ indicating a moderate fit, and for dye 4 a negative R^2 indicating poor fit, mostly because of the last predicted value of 10 ppm, however, the error is small in the region of interest around 1 ppm, hence, this does not represent a problem. However, since the decision of the system is based on a 1 ppm trigger, the measurement is taken in an area where the system is not saturated, and the results can be considered reliable, as summarised in **Table S5**.

Table S5: Calibration curve predictions, actual concentrations, and accuracy metrics for each dye. The actual calibration values are: 1, 2, 4, 6, 8, 10 ppm. Predicted concentrations are shown for each dye, along with Mean Squared Error (MSE) and the coefficient of determination (R^2).

Dye	**Predicted (ppm)**	**MSE**	**R^2**
Dye 1	0.978, 1.827, 4.599, 5.610, 7.788, 10.214	0.1053	0.9896
Dye 2	1.223, 1.877, 3.306, 5.883, 7.606, 12.749	1.3787	0.8640
Dye 3	0.540, 2.063, 4.194, 5.527, 9.321, 10.009	0.3702	0.9635
Dye 4	0.994, 2.046, 3.996, 5.609, 7.320, 17.997	10.7624	-0.0615
Dye 5	1.447, 1.710, 3.505, 5.456, 8.169, 11.238	0.3976	0.9608
Dye 6	1.076, 1.818, 3.648, 5.580, 9.907, 12.553	1.9008	0.8335

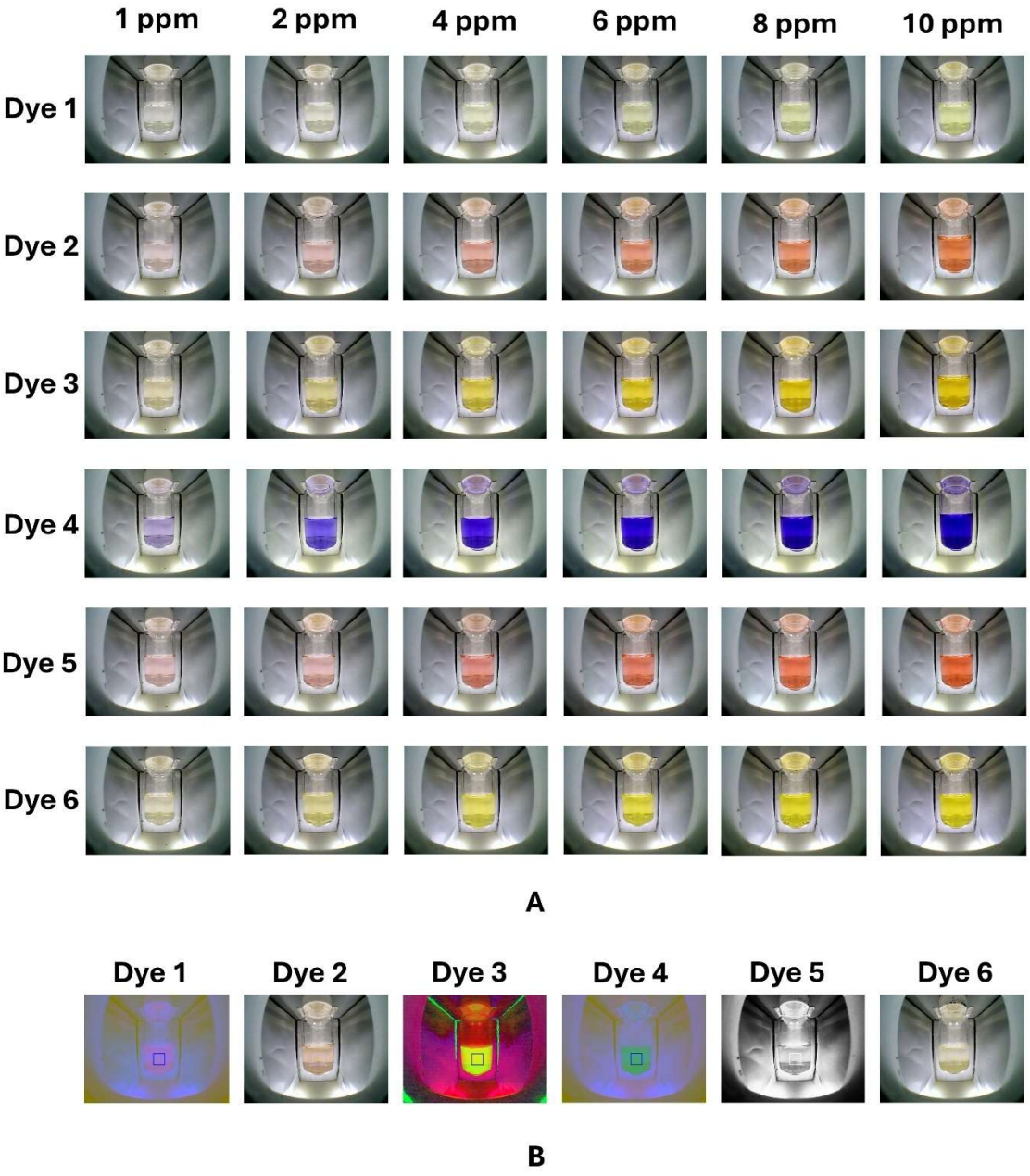

Figure S22: Calibration Samples and ROIs. A - Six calibration vectors of 1, 2, 4, 6, 8, and 10 ppm for each of the six dyes. B - The figure shows the selected channels for each dye: A from LAB, B from RGB, S from HSV, L from LAB, grayscale, and B from RGB, for dyes 1 to 6, respectively.

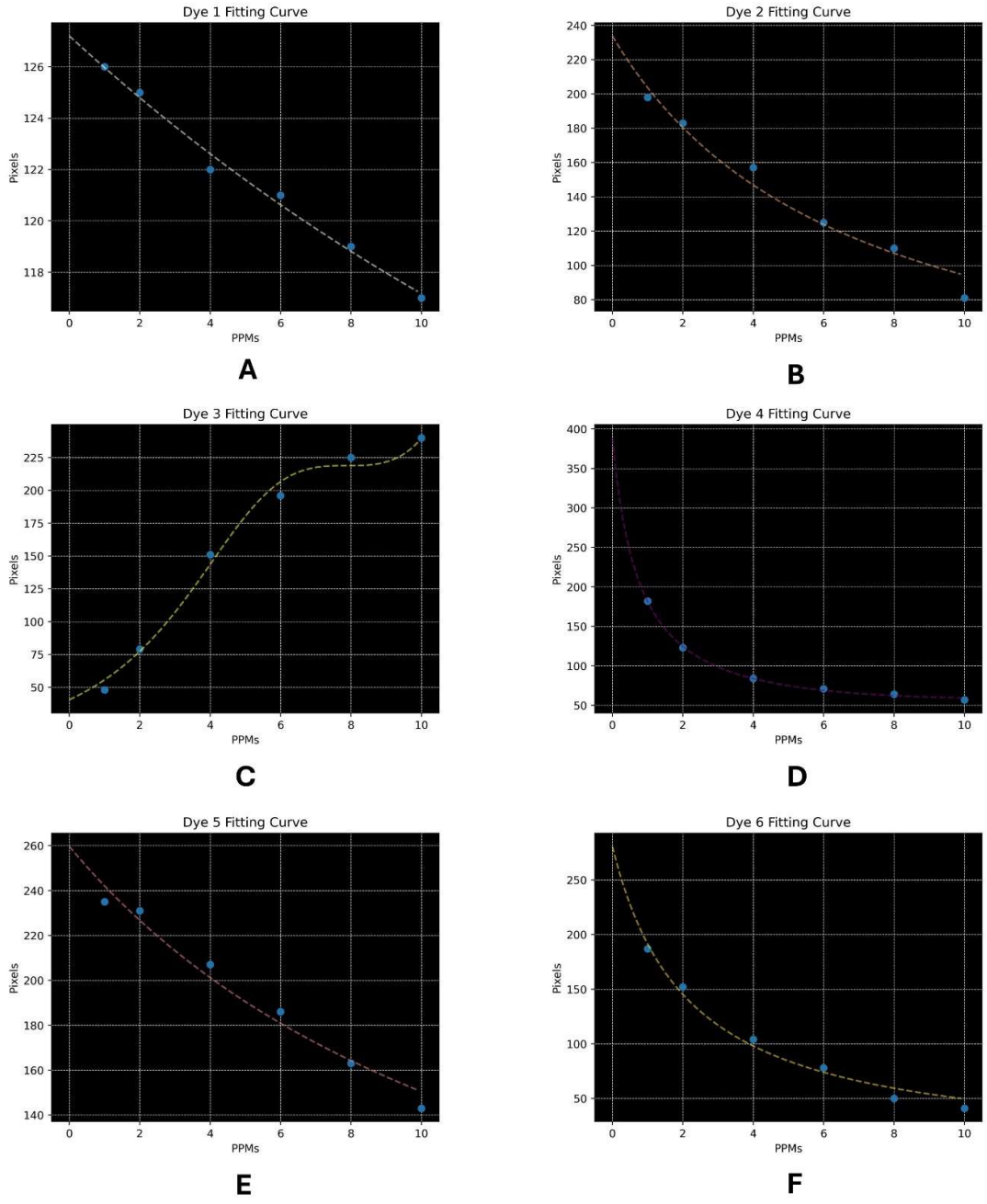

Figure S23: Curve Fits. A – Dye 1 shows a linear decreasing trend with concentration. B – Dye 2 shows an exponential decay. C – Dye 3 increases non-linearly in comparison to the other dyes; however, since the region of interest is around 1 ppm, this behaviour is acceptable. D – Dye 4 displays a sharp nonlinear decay. E – Dye 5 shows a moderate nonlinear decrease. F – Dye 6 follows an exponential decay, similar to dye 4.

3. Experimental Methods

3.1 Powder X-ray Diffraction

PXRD patterns were collected in transmission mode on a Panalytical Empyrean diffractometer equipped with an X-ray focusing mirror and a PIXcel3D detector in 1D lines can mode. Samples were mounted on Mylar film in a 96 well plate, in a hight-throughput stage. The radiation wavelength used was Cu-Kα (1.542 Å). Scan parameters were 2-40 ° 2θ scan range, with a 0.05° 2θ step size, and a 12-minute scan time.

3.2 ^{1}H NMR Spectroscopy

Solution ^{1}H NMR spectra were recorded at 400.13 MHz using a Bruker Avance 400 MHz NMR spectrometer. Referenced against the residual ^{1}H signal of the solvent.

3.3 ^{13}C NMR Spectroscopy

^{13}C NMR spectra were recorded at 100.6 MHz using a Bruker Avance 400 MHz NMR spectrometer.

3.4 High-resolution Mass Spectroscopy

HRMS was measured on an Agilent 6500 Series QTOF.

3.5 FTIR Spectroscopy

A Bruker Alpha-P ATR FTIR with a diamond crystal was used to collect IR data. The crystal was cleaned with ethanol, and a background was collected between every sample measurement.

3.6 UV/VIS Spectroscopy

All uv/vis spectroscopy data was collected using a Shimadzu UV-2600 I.

Section 4: Software Structure

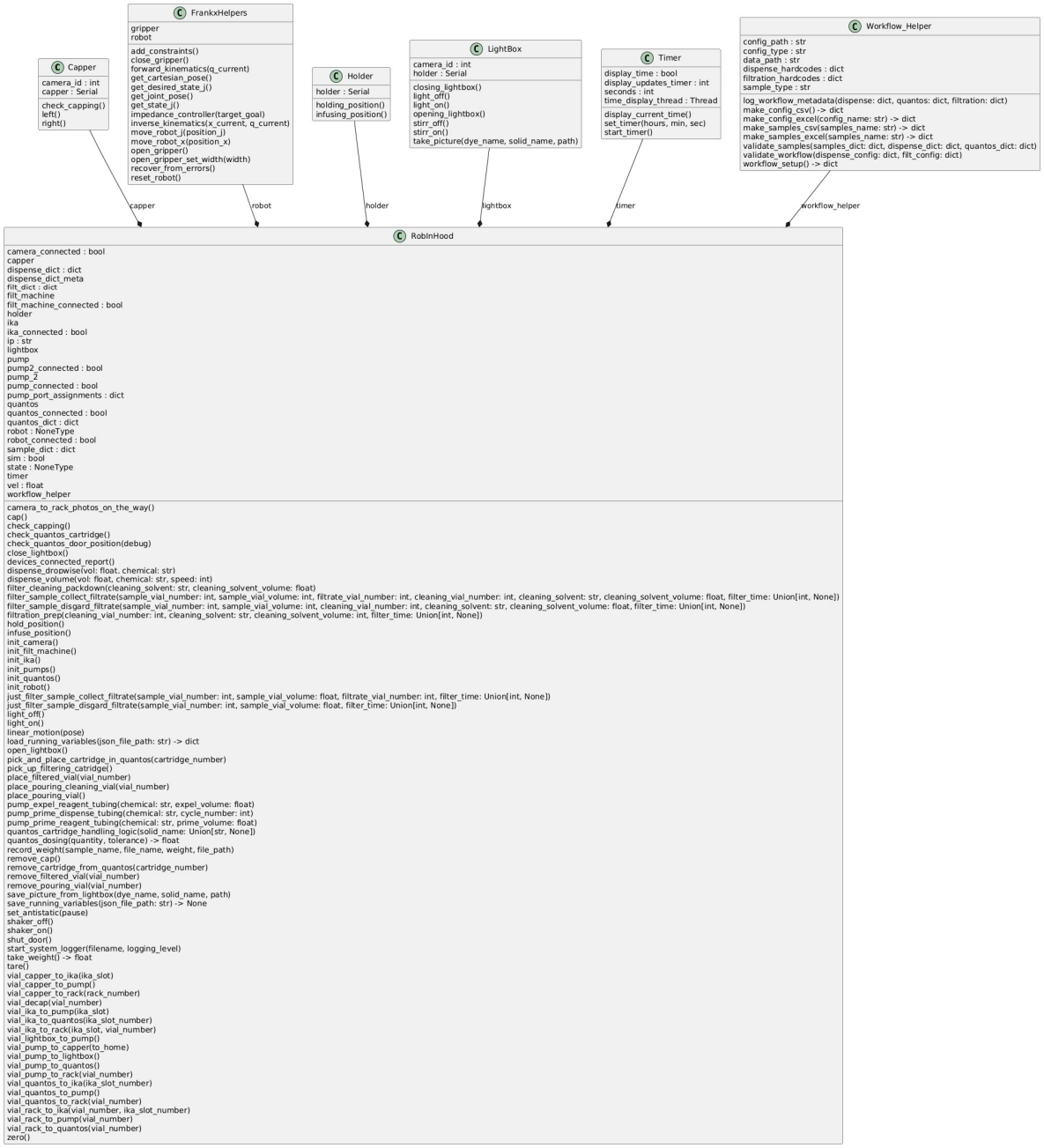

Figure S24: UML class diagram summarizing the structure of robinhood and the functionality of each of its components.

Section 5: Additional Experimental Details

Section 5.1 Dye-based porosity screening

Table S6: Porosity classification of materials based on dye uptake experiments. If the system predicted a dye concentration ≤ 1 ppm, it was counted as a hit.[4] A material was classified as **porous (1)** if two or more hits were observed across the six dyes; otherwise, it was classified as **non-porous (0)**.

Material Name (Figure Number)	**1 = Porous 0 = Non-porous**	**Dye 1**	**Dye 2**	**Dye 3**	**Dye 4**	**Dye 5**	**Dye 6**
CMP2_a (**Figure S25**)	0	0	0	0	0	0	0
CMP23_DMF (**Figure S26**)	0	0	0	0	0	0	0
CMP1_Toluene (**Figure S27**)	1	0	0	1	1	0	1
CMP2_THF (**Figure S28**)	1	0	0	0	1	1	1
CMP1_a (**Figure S29**)	0	0	0	0	0	0	0
Ni-BTC (**Figure S30**)	0	0	0	0	0	0	0
CC19 (**Figure 4**)	0	0	0	0	1	0	0
MIL-68(Al) (**Figure S31**)	1	0	1	1	0	0	1

Table S7: Porosity classification data from the previously reported work.[4] Reproduced here for ease of comparison. A material was classified as **porous (1)** if two or more hits were observed across the six dyes; otherwise, it was classified as **non-porous (0)**.

Material Name (Sample Number in [4])	**1 = Porous 0 = Non-porous**	**Dye 1**	**Dye 2**	**Dye 3**	**Dye 4**	**Dye 5**	**Dye 6**
CMP2_a (30)	0	0	0	0	0	0	0
CMP23_DMF (35)	0	0	0	0	0	0	0
CMP1_Toluene (29)	1	0	0	1	1	1	1
CMP2_THF (31)	1	0	0	0	1	1	1
CMP1_a (27)	0	0	0	0	0	0	0
Ni-BTC (45)	0	0	0	0	0	0	0
CC19 (23)	1	0	0	0	1	1	1
MIL-68(Al) (40)	1	0	1	1	1	1	1

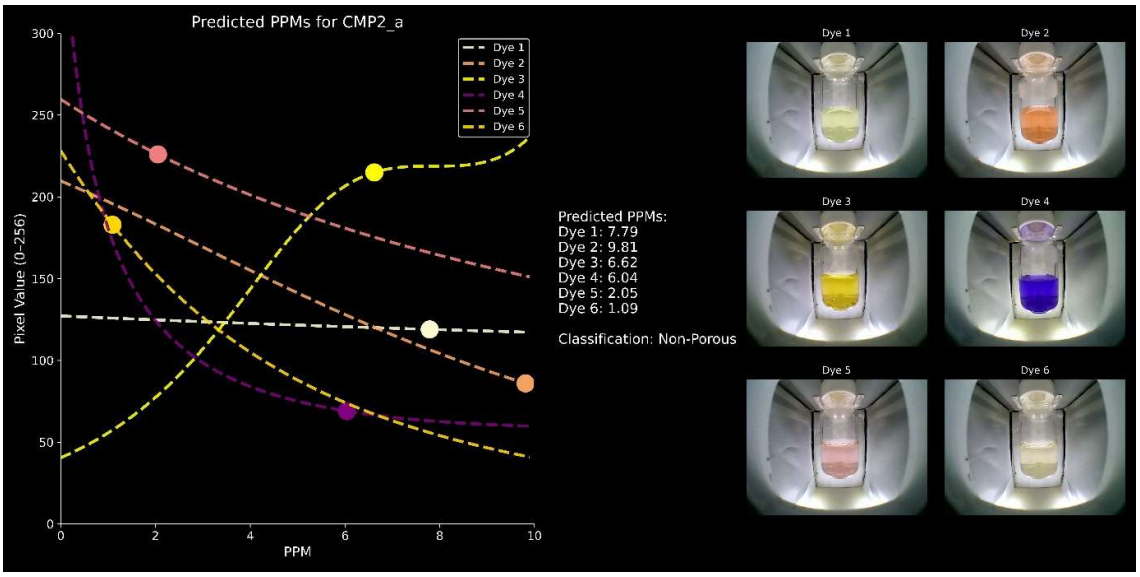

Figure S25: Visual results for CMP2_a. The samples remain coloured and therefore the material is non-porous.

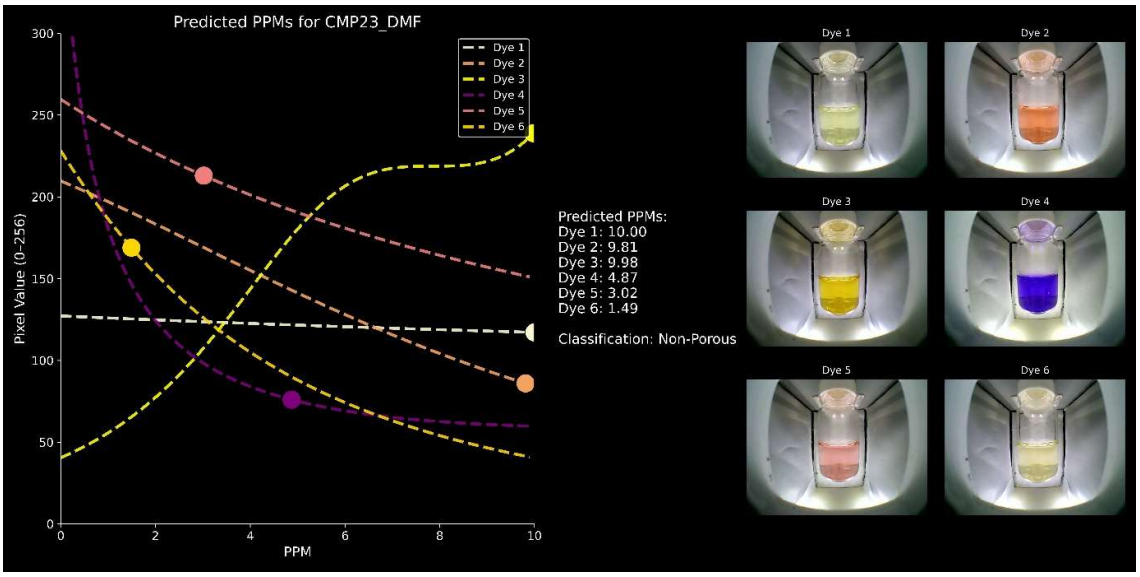

Figure S26: Visual results for CMP23_DMF. The samples remain coloured and therefore the material is non-porous.

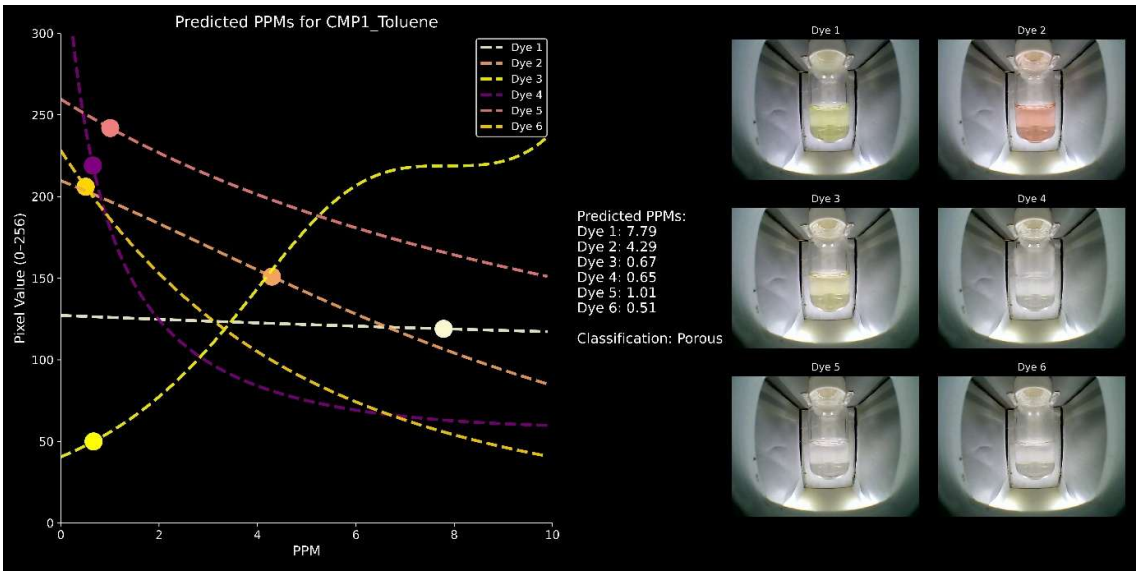

Figure S27: Visual results for CMP1_Toluene. There are three samples with 1 or less than 1 ppm. Therefore, the material is classified as porous.

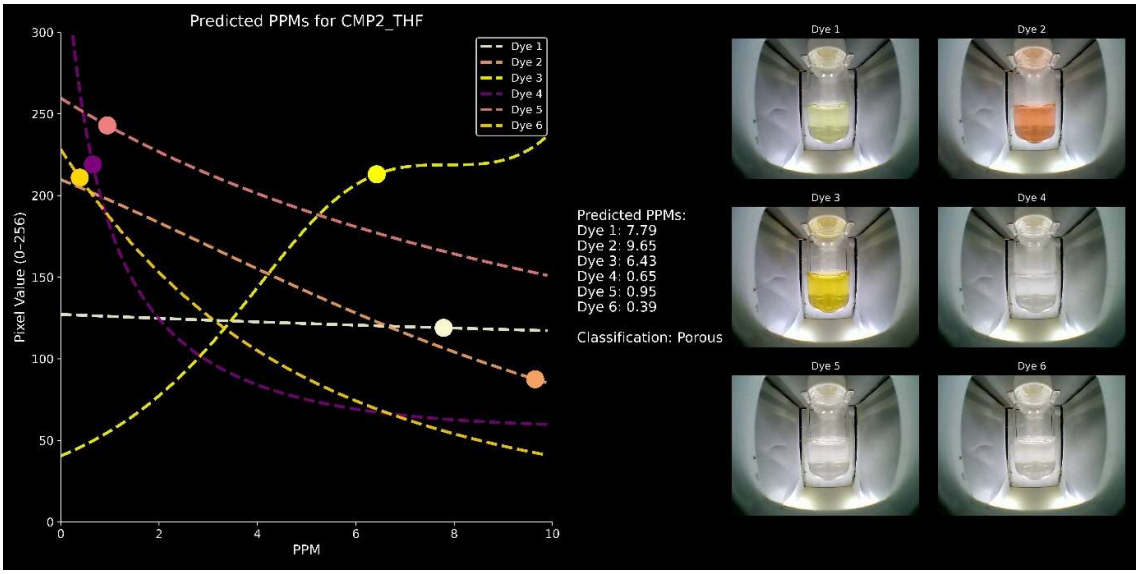

Figure S28: Visual results CMP2_THF. There are three samples with 1 or less than 1 ppm. Therefore, the material is classified as porous.

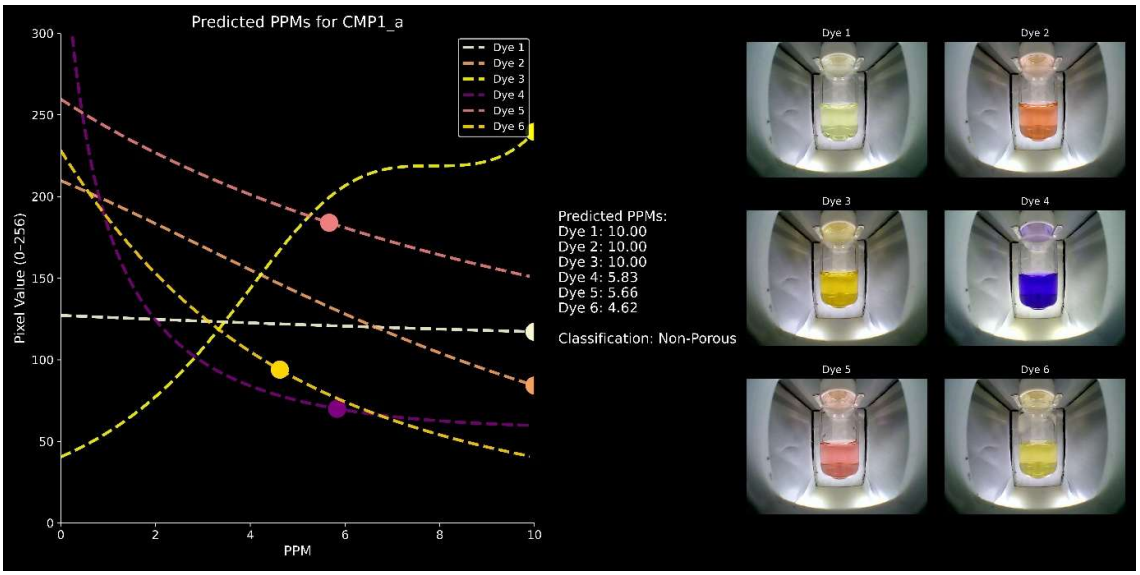

Figure S29: Visual results for CMP1_a. The samples remain coloured and therefore the material is non-porous.

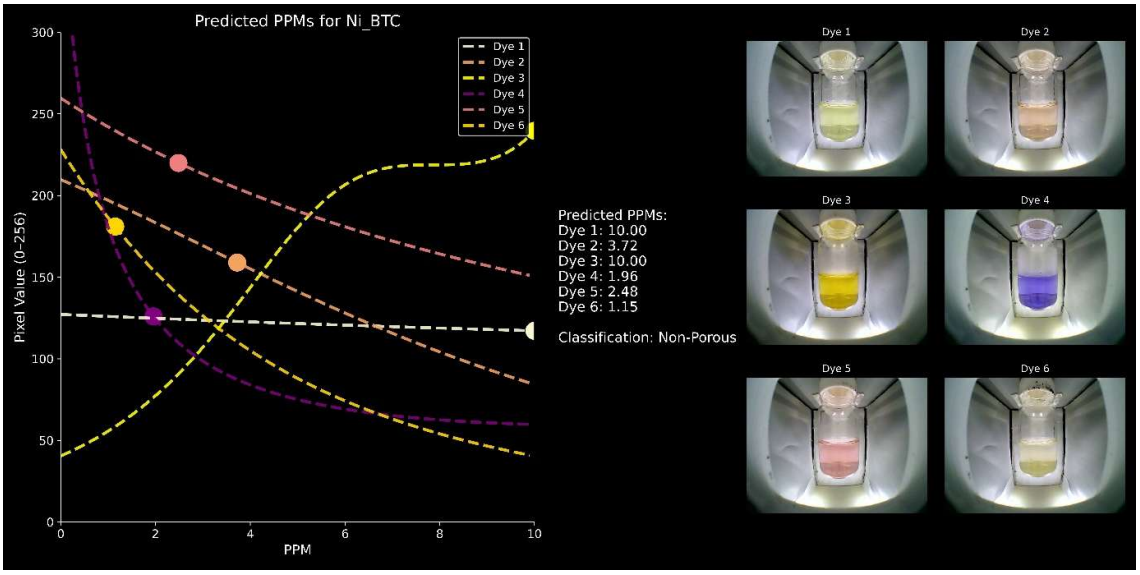

Figure S30: Visual results Ni BTC. The samples remain coloured and therefore the material is non-porous.

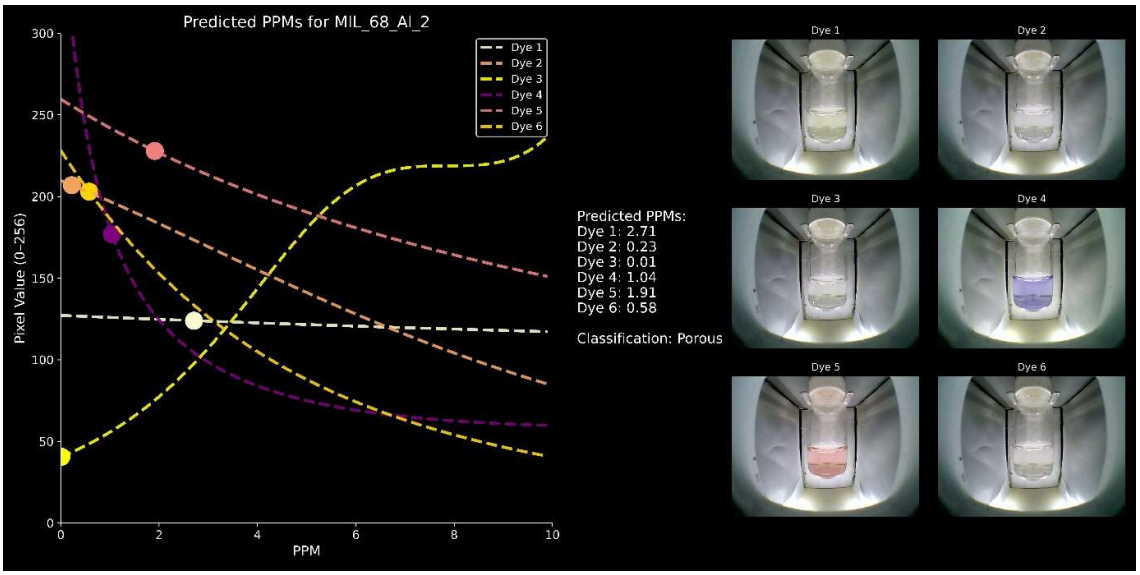

Figure S31: Visual results MIL_68_Al. There are three hits. Therefore, the material is classified as porous.

Section 5.2 Synthesis of CC3

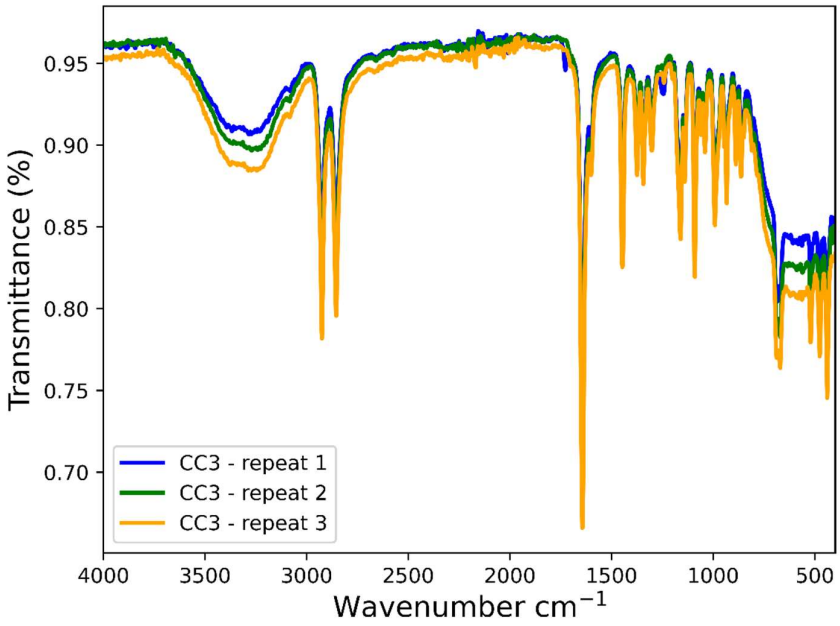

Figure S32: FTIR spectra of the three CC3 samples synthesised on RobInHood. Spectra were recorded on an FTIR Bruker Alpha. The spectra are a good match for the published spectra. [5] Small variations between spectra could be due to differing degrees of de-solvation, as this was also observed in published spectra.

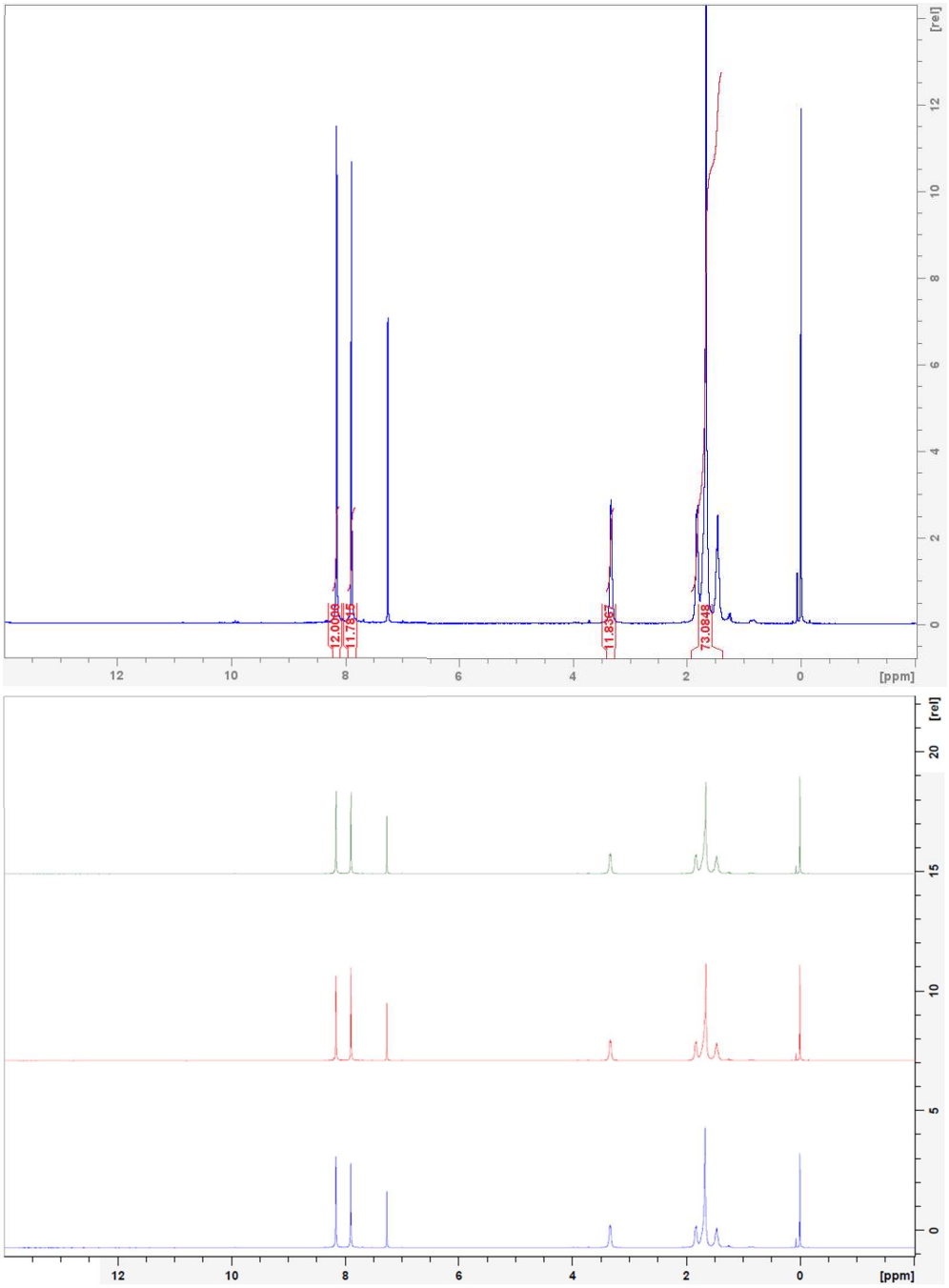

Figure S33: ^{1}H NMR (400 MHz, $CDCl_3$) spectra of the three CC3 samples synthesised on RobInHood. 8.16 ppm (s, C*H*=N 12 H), 7.90 ppm (s, Ar*H*, 12 H), 7.26 ppm (s, $CDCl_3$ [3]), 3.34 ppm (m, C*H*N, 12), 1.83-1.48 ppm (m, CH_2 73 H). A. Spectra of the first sample showing the integrated intensity of the CC3 peaks. B. Comparative spectra of all three samples. There is good agreement between the peak positions in these spectra with previous.[5] Moreover, the integra of the spectra at >1.83 ppm, also agree with previously reported values. However, the integrated intensity of the multiplet observed between 1.83-1.38 ppm was found to be 73 H, as opposed to the 48 H previously reported. In this case additional H in these positions are ascribed to either residual solvent or unreacted 1,2 – diaminocyclohexane.

Section 5.3 Synthesis of a phthalimide

HRMS was measured on an Agilent 6500 Series QTOF

Calculated for $C_{15}H_9N_2O_6^+$ [M+H](ESI): 313.0455, found: 313.0455

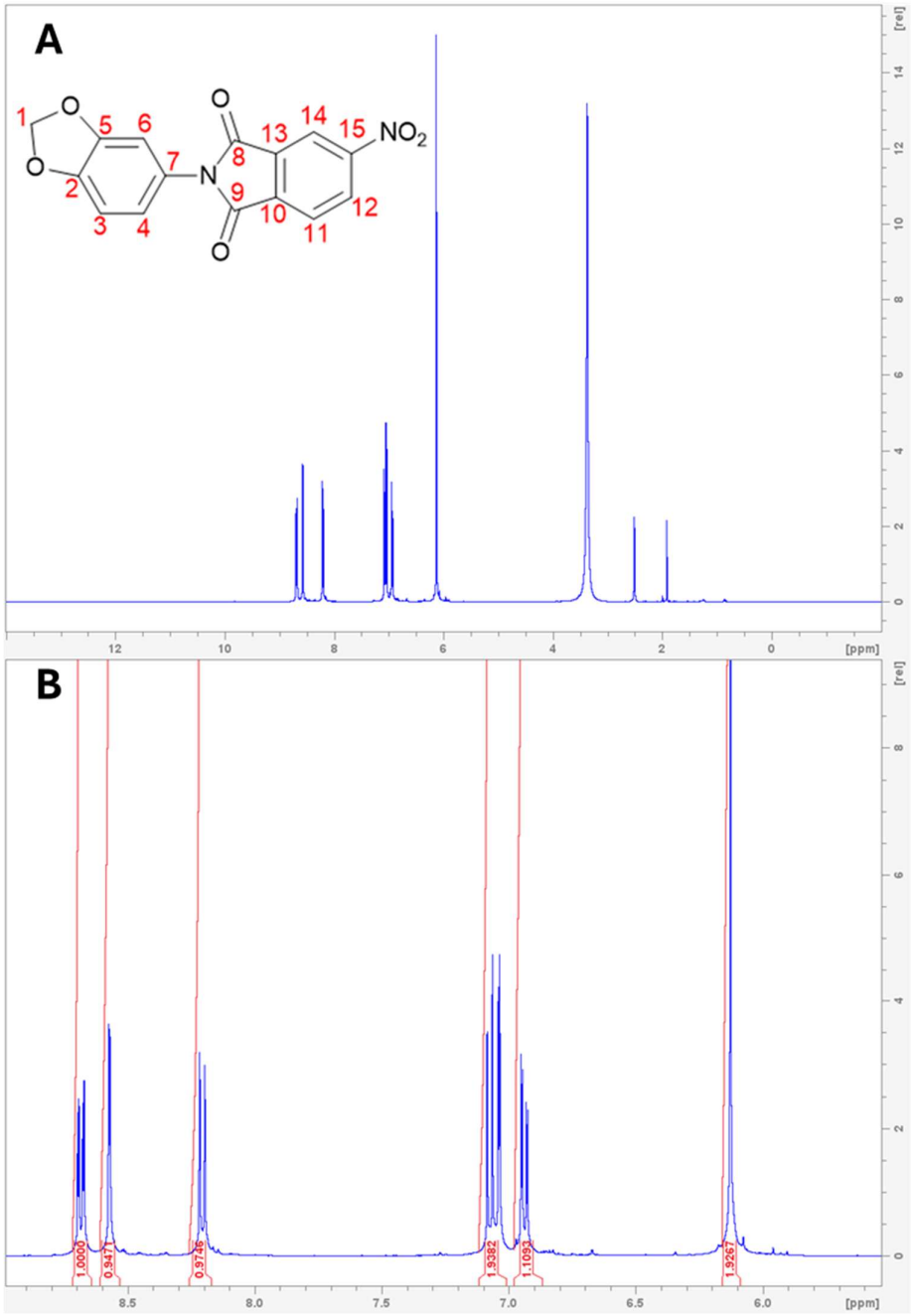

Figure S34: ^{1}H NMR (400 MHz, DMSO) δ 8.68 (dd, *J* = 8.1, 2.0 Hz, 1H, H_{12}), 8.56 (dd, *J* = 2.0, 0.4 Hz, 1H, H_{14}), 8.20 (dd, *J* = 8.2, 0.4 Hz, 1H, H_{11}), 7.12 – 7.01 (m, 2H, H_{3+6}), 6.98 – 6.87 (m, 1H, H_4), 6.12 (s, 2H, H_1). A. Full spectra with labelled assignment. B. Region of interest showing the peak integra.

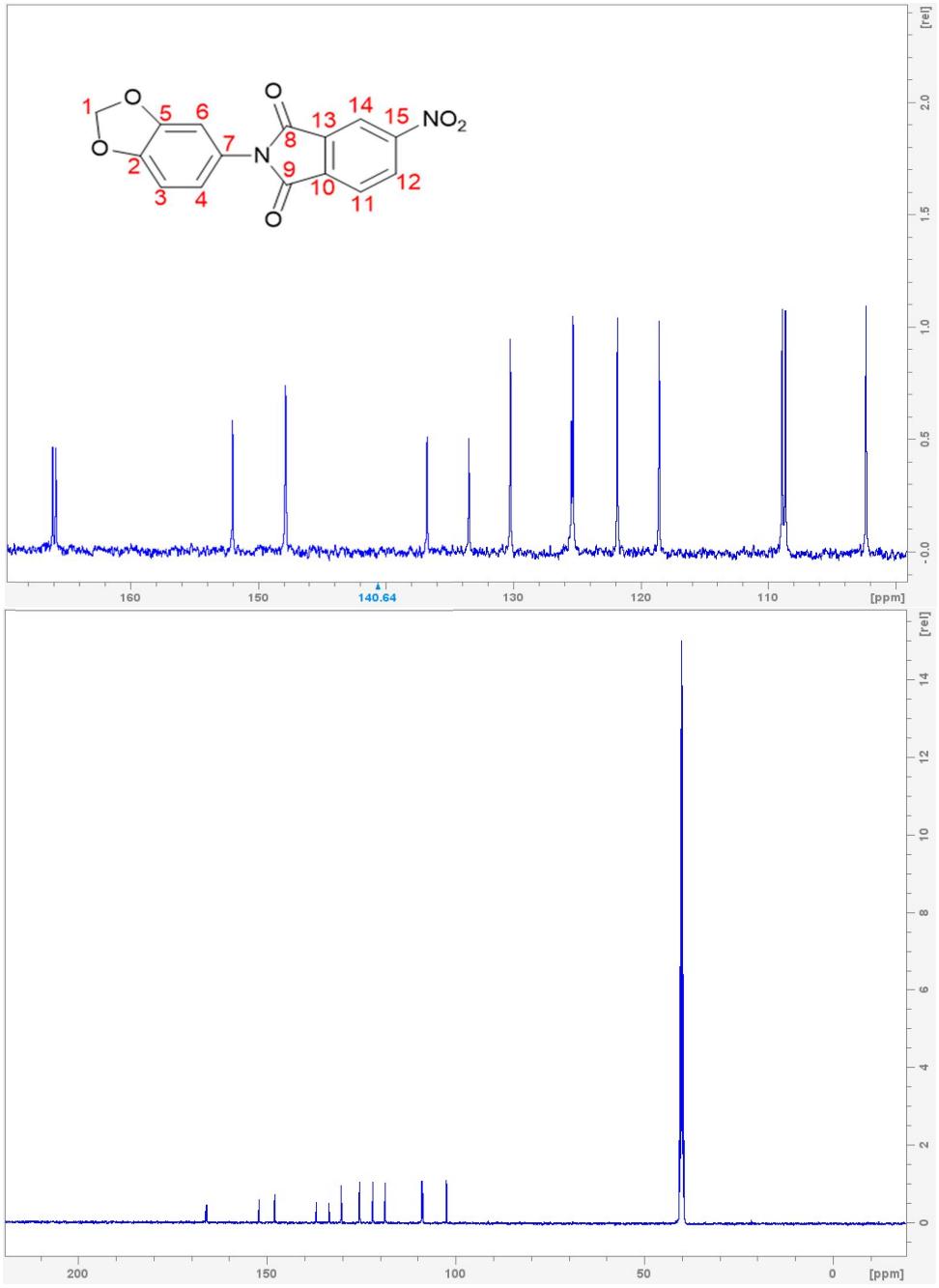

Figure S35: A. Region of interest with labelled assignment. B. Full spectra. ^{13}C NMR (101 MHz, DMSO) δ 165.64 (C_9), 165.39(C_8), 151.55 (C_{15}), 147.43 ($C_{2/5}$), 147.37($C_{2/5}$), 136.32(C_{13}), 133.04(C_{10}), 129.79(C_{12}), 125.00(C_7), 124.87(C_{11}), 121.39(C_4), 118.12(C_{14}), 108.46(C_6), 108.20(C_3), 101.88(C_1).

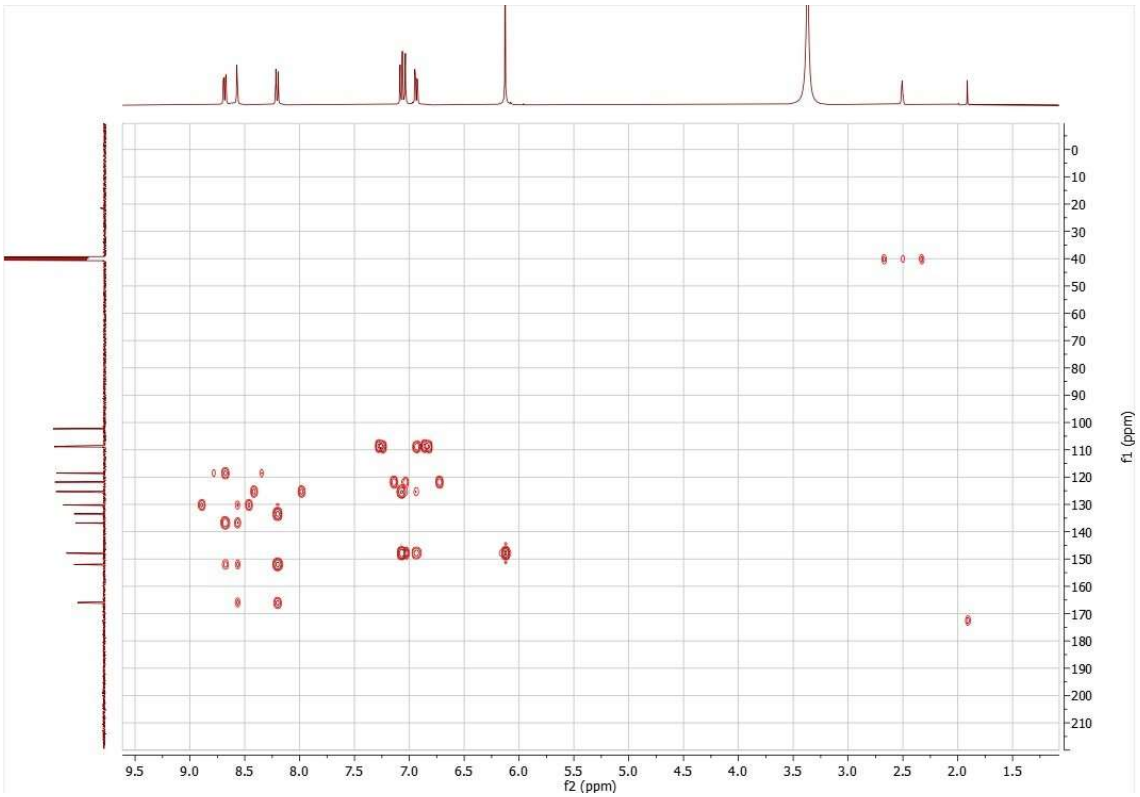

Figure S36: $^{1}H–^{13}C$ HMBC spectrum of the phthalimide compound in DMSO-d6.

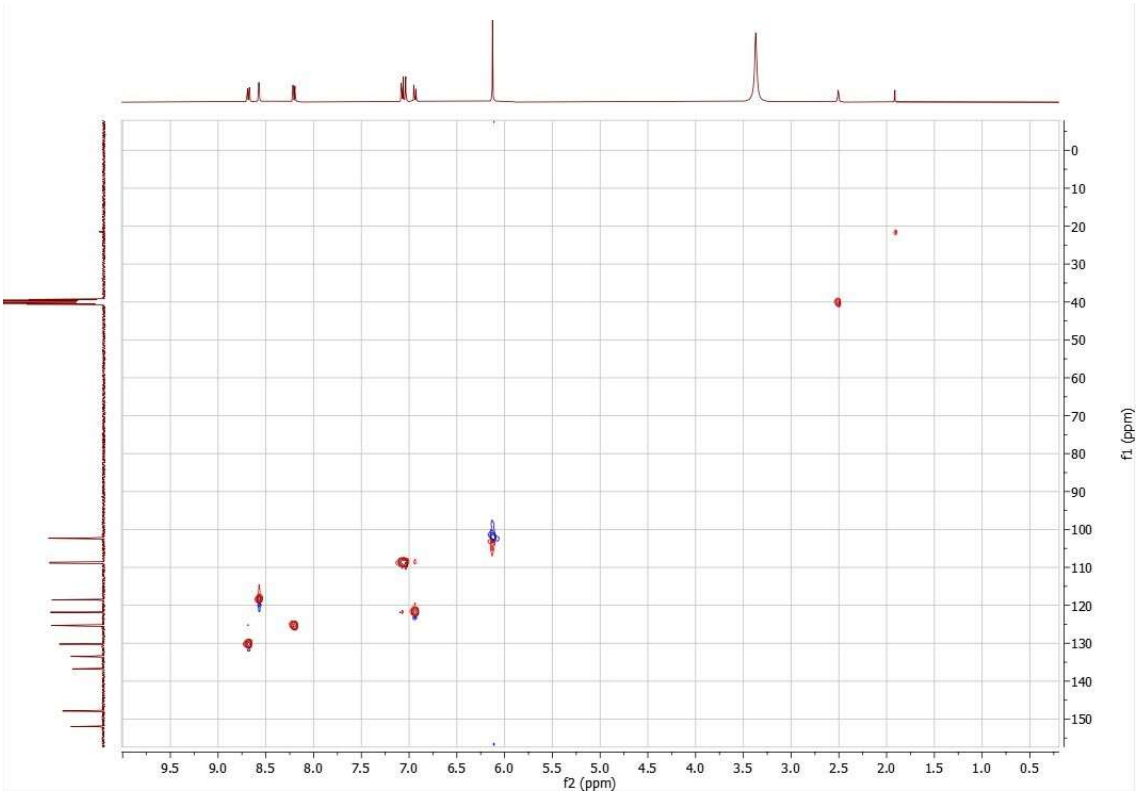

Figure S37: $^{1}H–^{13}C$ HSQC spectrum of the phthalimide compound in DMSO-d6

6. Supporting Information References:

1. Munguia-Galeano F, Longley L, Veeramani S, Zhou Z, Clowes R, Fakhruldeen H, et al. An Open-Source Capping Machine Suitable for Confined Spaces. In: Cavalcanti A, Foster S, Richardson R, editors. Towards Autonomous Robotic Systems. Cham: Springer Nature Switzerland; 2026. p. 461–74.

2. W. Wagner, A. Puss. The IAPWS Formulation 1995 for the Thermodynamic Properties of Ordinary Water Substance for General and Scientific Use. J Phys Chem Ref Data. 2002;31:387–535.

3. Fulmer GR, Miller AJM, Sherden NH, Gottlieb HE, Nudelman A, Stoltz BM, et al. NMR chemical shifts of trace impurities: Common laboratory solvents, organics, and gases in deuterated solvents relevant to the organometallic chemist. Organometallics. 2010;29(9):2176–9.

4. Han Y, Borne I, Dutta B, Clowes R, Qu H, James A, et al. Accelerated Porosity Screening Using a Multichannel Colorimetric Array. Angew Chem Int Ed [Internet]. 2025 Aug 21 [cited 2025 Sept 1];137(40). Available from: https://onlinelibrary.wiley.com/doi/10.1002/anie.202510400

5. Tozawa T, Jones JTA, Swamy SI, Jiang S, Adams DJ, Shakespeare S, et al. Porous organic cages. Nat Mater. 2009 Dec;8(12):973–8.